2022-01-0497 Published 29 Mar 2022

Bulk Spray and Individual Plume Characterization of LPG and Iso-Octane Sprays at Engine-Like Conditions

Brye Windell and Manav Sharma Colorado State University

Lorenzo Nocivelli and Katherine Asztalos Argonne National Laboratory

Andrew Zdanowicz, Tanmay Kar, Daniel Olsen, Anthony Marchese, and Bret Windom Colorado State University

Citation: Windell, B., Sharma, M., Nocivelli, L., Asztalos, K. et al., "Bulk Spray and Individual Plume Characterization of LPG and Iso-Octane Sprays at Engine-Like Conditions," SAE Technical Paper 2022-01-0497, 2022, doi:10.4271/2022-01-0497.

Received: 27 Jan 2022 Revised: 27 Jan 2022 Accepted: 19 Jan 2022

Abstract

This study presents experimental and numerical examination of directly injected (DI) propane and iso-octane, surrogates for liquified petroleum gas (LPG) and gasoline, respectively, at various engine like conditions with the overall objective to establish the baseline with regards to fuel delivery required for future high efficiency DI-LPG fueled heavy-duty engines. Sprays for both iso-octane and propane were characterized and the results from the optical diagnostic techniques including high-speed Schlieren and planar Mie scattering imaging were applied to differentiate the liquid-phase regions and the bulk spray phenomenon from single plume behaviors. The experimental results, coupled with high-fidelity internal nozzle-flow simulations were then used to define best practices in CFD Lagrangian spray models. Optical imaging revealed that unlike iso-octane, propane's spray propagation was fed by its flash boiling, spray collapse, and high degree of vaporization, resulting in a direct proportionality of propane's penetration length to temperature. These unique features of propane and its variation from iso-octane's spray pattern, contributed to its classification as an unconventional spray. Appropriate corrections to the injection and breakup models were developed to reproduce the under-expanded jet dynamics and to mimic the flash boiling-driven spray development observed with propane sprays. The simulation results were found to be sensitive to cone and inclusion angles of the blob injector. The current work represents a first assessment of the capability of the commonly available models for engine-spray simulations and highlights the fact that, despite the reasonable agreement obtained in the fuel vapor morphology, the representation of the liquid phase lacks accuracy and requires further model development.

Introduction

Owing to the awareness of the environmental issues related to fossil fuels and recent changes to greenhouse gas (GHG) emission standards worldwide, efforts are being focused on advancing current combustion technology and alternative transportation options. Since 1992, the United Nations established the "Framework Convention on Climate Change" to formally address GHG reduction, concerns regarding CO_2 emissions have increased [1]. The United States' goal to reach net zero emissions economy-wide by 2050 indicates that all energy sectors need to make efforts to reduce GHG emissions [2]. While the passenger vehicle industry is rapidly shifting focus towards electrification, the high initial cost combined with a lack of charging station infrastructure is still a significant hurdle to overcome in the heavy-duty sector [3]. In response to this, automobile companies have focused on hybrid and diesel vehicles to meet emission regulations and improve fuel economy at the same time [1, 2].

Internal combustion engine (ICE) research focuses on the improvement of fuel economy and the reduction of the tailpipe emissions of CO_2 and other regulated pollutants. Fuels such as LPG are promising solutions. LPG represents a practical and economical solution for fueling the United States' heavy-duty transportation sector. LPG, primarily composed of propane and butane, is a byproduct of natural gas processing and liquid petroleum refining. The United States maintains a substantial surplus of LPG despite being the largest exporter. Based on average commodity prices from 2019, LPG cost is approximately 40% less than gasoline and diesel per gasoline gallon equivalent [4]. LPG has a significantly higher H:C ratio than diesel and gasoline, ultimately reducing GHG emissions if equivalent energy conversion efficiencies can be achieved. Furthermore, LPG offers combustion advantages over many traditional fuels including a higher octane rating (RON ranging from 95-109.4 for a variety of global LPG blends vs. 84-93 for gasoline), than traditional gasoline fuels and higher

flame speeds than natural gas [5, 6]. LPG is stored as a liquid at moderate pressures and, as such, has significantly higher energy densities compared to CNG (~27 MJ/L for LPG @ 350 psi vs. 9 MJ/L for CNG at 3,600 psi) [7]. Therefore, LPG would require fewer updates to current refueling infrastructure than CNG. There is also considerable interest in blending LPG with renewable dimethyl ether (DME) as a way to further reduce the fuel's environmental impact. Given these attributes, LPG represents a practical, economical, and more sustainable solution for fueling the United States heavy-duty transportation sector. However, before widespread adoption can occur, energy conversion efficiencies for LPG engines must achieve values comparable to those seen in diesel engine platforms. The overarching goal of the research is to address fundamental limitations to achieve near-diesel efficiencies in heavy-duty on-road LPG engines. To achieve comparable energy conversion efficiencies as seen in diesel engine platforms, the injection technique of LPG plays a crucial role in the development of LPG engines.

Direct injection has gained considerable traction in the industry due to its proven fuel efficiency benefits over conventional, port fuel injected engines by enabling down sized boosted engine architectures [8, 9]. Recent advancements in high-pressure GDI fueling systems have made DI more viable. When used together, DI and propane-fueling technologies provide a pathway towards significantly increased efficiency and decreased emissions. The role of the fuel injection systems in GDI engines is to achieve a suitable fuel vapor distribution, homogeneous or with some degree of stratification, while avoiding unwanted effects such as wall wetting. Therefore, it is desirable to characterize the fuel injection systems and the fuel vaporization and dispersion in the combustion chamber to investigate and improve the combustion process. Spray breakup and vaporization processes are affected by the fuel's volatility and viscosity [10]; LPG due to its unique physical properties, namely high vapor pressure, high volatility and low viscosity, will likely require modifications to injection hardware and combustion chamber designs as well as different operation strategies (injection timing, pulse duration, number of injections, etc.) to enable efficiencies greater than those experienced by current state of the art gasoline DI systems. Hence, more research is needed to study LPG and characterize its mixing processes before it can be adapted to current DI engines. An improved understanding of the mechanisms that govern the fuel spray will enable the development of tractable and high fidelity simulations that can support the design of the fuel injection systems required by high efficiency LPG engines.

The implementation of accurate injection models has become a pivotal design and optimization tool for DI fueled engines. The Lagrangian spray modeling approach allows for the simulation of engine-sized domains since it avoids the detailed solution of the liquid-gas interface dynamics by treating the spray as a cloud of discrete parcels that are tracked in their trajectory and coupled with the gas phase [11]. For this reason, it relies heavily on semi-empirical modeling to define the injection characteristics, the jet evolution, and the fuel's phase-change. By definition, this approach considers the spray as an incompressible fluid and, in its conventional definition, it lacks accuracy in the representation of under-expanded jets such as propane operated in engine-like conditions [12, 13]. The representation of the expansion of flare flashing gasoline sprays has been correctly represented, informing the Lagrangian parcel injection model with results from detailed nozzle flow simulations, and by adding additional vaporization terms [14]. This framework represents the baseline for the development of propane spray models, which show extreme volatility, and referring to recent work on gasoline sprays [15], the effect of flash boiling on the jet breakup is further implemented by modifying the characteristic droplet size reduction trends. The end goal of the spray modeling development for engine applications is represented by the correct prediction of the liquid phase penetration to prevent wall wetting, and the proper representation of the fuel entrainment in the combustion chamber. These features are relevant to capture the performance and the emission propensity of the engine operation and are usually based on preliminary correlation studies in a constant volume inert environment.

Limitations to achieve higher efficiency engines involve engine knock, misfires, low emissions limits, and the wide range of chemical reactivity in LPG. In the United States, LPG used in vehicles is typically specified as HD-5 propane, a 90 % mixture of propane (C_3H_8) with smaller or trace amounts of other gases. On the global market, LPG composition can vary dramatically from the HD-5 propane specification, leading to even more insufficient experimental data for model validation [10]. Since propane, the principal component of LPG, is prone to flash-boiling at normal GDI engine operation conditions compared to traditional fuels used in DI [16], it is essential that the spray models capture the unique effects seen in LPG sprays. The dramatic differences in volatility lead to significantly more flash boiling seen in LPG sprays as compared to gasoline. As a result, the liquid/vapor penetration lengths of LPG are highly sensitive to the engine conditions at the time of fuel injection. As such, for optimizing DI using LPG, finding the ideal coupling between the in-cylinder fluid motion, timed injection events, and robust spray models validated by experimental data capable of predicting LPG spray behaviors over a range of operating conditions is required [7]. Liquid and vapor spray morphologies, as well as penetration trends, are therefore targeted in this study as major validation parameters to build a reliable and accurate spray model.

To date, many studies have investigated the behavior of gasoline, diesel, a variety of surrogates and alcohol fuels using Mie Scattering and Schlieren imaging techniques to visualize spray development and species/phase distributions during cold injection and combustion events [17-23], however, only a limited number of validated spray models [24-26] and experimental data [10, 27] are available regarding the spray dynamics of LPG at engine-relevant conditions. In [10] Mie Scattering and Schlieren were applied to study LPG and iso-octane sprays where global spray characteristics, including spray angle, spray liquid and vapor penetration lengths are presented for multiple spray/fuel and chamber conditions. While the data provides valuable information regarding the overall spray behaviors, it is difficult to extract plume specific information, which is critical for spray model validation. Similar to this previous work, this project seeks to develop an experimental setup for visualization of LPG sprays, with an added emphasis on using

planar laser Mie scattering to map out the liquid regions for an individual plume and using this data to develop, validate, and tune a numerical LPG spray model for use in full cycle engine simulations. This work as part of a larger effort seeks to support the design of heavy-duty DI-LPG engines with energy conversion efficiencies comparable or greater than state of the art diesel engine platforms.

Methods

In order to isolate the spray phenomena from in-cylinder flows, alternative test facilities such as a constant volume chamber are often employed. The simple operation and convenient optical access of this facility makes it attractive for controlled investigations that can be used to validate physics-based models and provide important insight into spray processes. This facility provides a fixed volume of trapped gas, which is inert and quasi-quiescent. It, therefore, allows for the study of spray phenomena isolated from the complex in-cylinder turbulence and combustion. The constant volume high-pressure spray chamber (HPSC), marked A in Figure 1a, is designed and optimized to primarily simulate conditions encountered in the combustion chamber of advanced direct injection, spark ignition engines.

FIGURE 1 (a) HPSC setup assembly including (A) high-pressure spray chamber, (B) Spray-G fuel injector and a custom fuel rail, (C) syringe pump, (D) large engine control module, (E) propane tank, and (F) Nd: YAG laser, (b) HPSC solid model, and (c) a schematic describing working of the fuel injector and the water jacket.

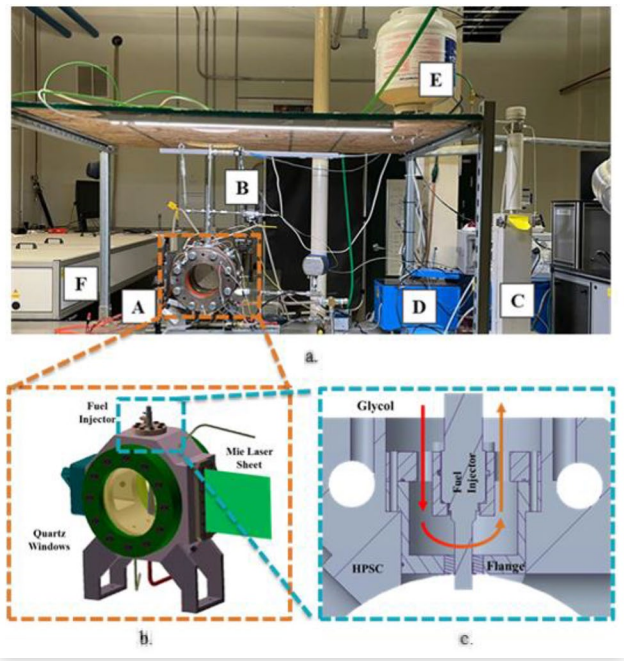

The Spray Facility

Figure 1b shows the solid model of the HPSC. As shown, the HPSC is designed to allow 3 - way optical access inside the chamber using UV-grade fused silica windows (front and back windows with a diameter of 150 mm, and a 150 mm-tall square window on the side). This configuration allows for both line-of-sight and orthogonal visualization of the fuel spray.

The fuel injector was mounted vertically on the top of the chamber using a custom fuel rail and a fixture that incorporated a temperature-controlled water jacket, as seen in Figure 1a. The water jacket can heat the fuel to a desired temperature by utilizing a circulating pump, a 1 kW heater, a temperature controller, and a thermally insulated bath of glycol, as seen in Figure 1c, accurately within −0.5 to 4.7 K of error. The injector was pressurized using a ISCO 360D high-pressure syringe pump (labeled C in Figure 1a). The ambient pressure inside the HPSC was regulated using pressurized nitrogen gas and a vacuum pump, well within the margin of experimental error. The HPSC was fitted with an absolute pressure transducer and thermocouples mounted on the metal block of the chamber to monitor and acquire the instantaneous chamber conditions through a LabVIEW virtual instrument interface. The corresponding temperature was controlled via high-power-density cartridge heaters embedded in the body of the HPSC and tape heaters wrapped around the silica windows, within −5 to 10 K of error. Before each injection event, the HPSC was purged with pressurized nitrogen gas to inhibit the oxidation of the fuel, making the ambient conditions non-reactive. A combination of o-rings and gaskets were used to seal the chamber under high ambient pressures.

The Spray G fuel injector is an experimental, Delphi manufactured, axisymmetric, 8-hole, solenoid driven, GDI fuel injector. The Spray G AV67-012 DI fuel injector provided by the Engine Combustion Network (ECN) has been used extensively in prior literature and has been well characterized [28-31]. The fuel injector was driven by Woodward's Large Engine Control Module (LECM), marked D in Figure 1a, to control the electronic injection duration. The LECM was programmed to produce an electronic injection duration of 680 µs after the start of injection (ASI). But 870 µs ASI was the actual injection duration that was measured using Schlieren imaging synced to an oscilloscope. The injector was pressurized using a high-pressure syringe pump labeled C in Figure 1a. The temperature around the injector tip was regulated by flowing glycol through the water jacket as shown in Figure 1c.

Optical Diagnostics

To compare the experimental data collected using optical diagnostics techniques and the numerical spray simulations, a set of parameters including vapor and liquid spray penetration lengths, widths, and speeds, were utilized to map out the spray morphology for an effective qualitative and quantitative comparison and model validation. These measurements were collected at engine-like conditions using imaging techniques such as high-speed Schlieren and planar Mie scattering.

High-Speed Schlieren Imaging Schlieren imaging is a well-established, line-of-sight technique that is commonly used to visualize inhomogeneities in the refractive index of a transparent medium, created by gradients in the corresponding density field. This technique is commonly used in literature for both qualitative visualization and quantitative fuel spray measurements, such as vapor phase penetration [10, 12, 23, 32].

Figure 2a demonstrates a schematic of the high-speed Schlieren setup used to visualize the fuel injection events. A continuous, 200-lumen white LED was collimated through the HPSC by a 150 mm parabolic mirror of 750 mm focal length and received by an identical parabolic mirror placed in a z-type configuration. A knife-edge was used as the Schlieren cut-off at the focal point of the converging mirror to amplify the contrast and intensity variations. The images were finally sized with a 50 mm plano-convex achromatic lens of 150 mm focal length and acquired using a Photron FASTCAM SA5 high-speed camera. The corresponding imaging frequency was set to 30,000 frames per second, i.e., 33 µs between frames, to record Schlieren images free of undesired flow features, e.g., dynamic pressure waves. The high-speed Schlieren images, with a spatial image resolution of 298 µm/px capturing 376 x 640 pixel images, were recorded for a range of chamber and fuel conditions to study the axial vapor penetration length, width (as shown in Figure 2c), and penetration rate of the spray. An external delay generator was deployed to sync the Spray G injector and the Photron camera.

FIGURE 2 (a) Schematic of the top-view of Schlieren imaging setup, (b) Spray-G injector nozzle-alignment relative to the LED light, and (c) resulting Schlieren spray image, features, and nomenclature.

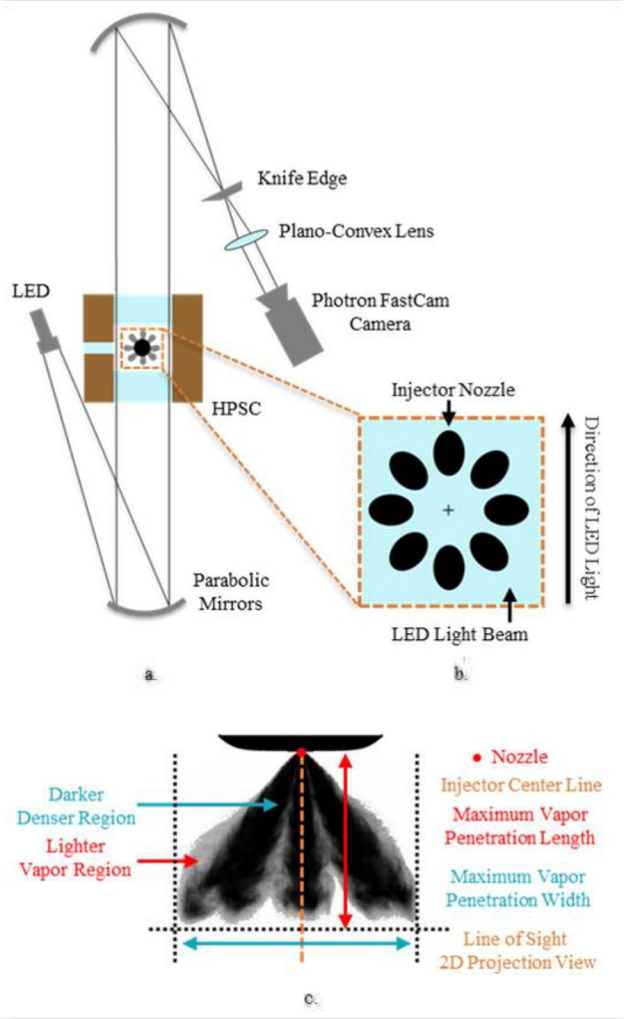

Schlieren images were scaled within experiment and between experiments to have a consistent light intensity for the entire data set and compensate for any light fluctuations caused by the LED. Once scaled, the background from each experiment was subtracted from the respective set of experiments, to define the boundaries of the spray clearly. However, background subtraction produced undesired artifacts in the spray core of the image, which was fixed by replacing the non-zero pixels of the image by the corresponding original raw image pixels. This helped to enhance the resolution and fix spray defects with minimal manipulation to raw data. Once processed, maximum axial vapor penetration lengths and maximum normal penetration widths, as seen in Figure 2c, were measured using simple edge finding algorithms in MATLAB, and plotted with respect to time. The vapor penetration speed was calculated by taking a first-order derivative with respect to time of the formally measured maximum penetration lengths. Three tests were taken for each test condition and the collected data was averaged to capitalize repeatability and increase accuracy of the measurements; the spray was imaged for 1200 µs ASI for each condition. These measurements help to provide detailed quantitative analysis in addition to the qualitative Schlieren images characterizing the spray morphology.

It is important to note, Schlieren provides a global image of both vapor and liquid regions of the spray. Therefore, the 3-dimensional spray structure of an 8-hole injector (Figure 2b) is accumulated into one plane, decreasing plume-to-plume distinction and resolution. Another key feature of Schlieren is that the light intensity gradients correspond to the density gradients in the spray. This, however, becomes challenging for a multi-phase spray, for a fuel such as propane, as no clear distinction between liquid and vapor regions can be observed, as seen in Figure 2c. Hence, Schlieren is used as a preliminary imaging technique to visualize the overall spray morphology but, also introduces the need for an advanced diagnostic technique to compensate for mentioned limitations of Schlieren imaging.

Planar Mie Scattering Imaging Mie scattering imaging is an elastic light scattering technique used extensively in prior literature to measure liquid penetration through a medium. When a spray is exposed to a specific wavelength of light, the liquid region scatters light in all directions, but the vapor regions do not illuminate. Hence, Mie scattering imaging is often used to capture the liquid regions of the spray [12, 16, 33, 34]. Coupled with Schlieren imaging, Mie can provide a strong comparison amongst the liquid regions, high density vapor regions, and low-density vapor regions. Like Schlieren, Mie scattering captures the liquid regions of the spray globally, i.e., no clear distinction between each plume can be observed. This study utilizes planar Mie scattering to

increase the plume-to-plume distinction and enhance the resolution of individual plume penetration morphology.

A custom Nd: YAG laser was used to produce a 532 nm beam with 25 ns pulse width and 7 mJ of energy per shot. The setup for Mie testing consisted of two 50 mm Nd: YAG mirrors designed to reflect 532 nm light to the height of the injector tip. The setup also included two cylindrical optics: a converging lens with a focal length of 1000 mm, and a diverging lens with a focal length of -75 mm as shown in Figure 3a, to create a thin laser sheet, 100 µm thick, bisecting the front nozzle of the fuel injector as seen in Figure 3b. The Mie laser sheet in Figure 3c was used to precisely image the spray structure of the individual plumes injected by the front and back nozzles in the plane of the laser sheet, represented in Figure 3d. Additional optics and equipment were used to regulate and measure the energy of the laser sheet, to finely tune the amount of energy delivered to the spray.

An Andor iStar sCMOS camera was used along with a Vivitar 75-300 mm macro focusing camera lens to capture the spray image with a spatial resolution of 49 µm/px and image size of 2560 x 2160 pixels at various instances of time, ranging from 25 µs to 1200 µs ASI. Similar to the Schlieren timing setup, the camera, the fuel injector, and the laser were synchronized using the external delay generator triggered by the LECM. The actual laser and camera shot timings relative to the start of injection were measured using an oscilloscope and was found to be within ± 15 µs. The Andor camera was gated for 15 ns to capture the center of the laser pulse.

The collected 16-bit Mie images were processed using a set of standard multi-step image processing techniques. It was observed that the laser energy had a gaussian distribution along the axis of injection; to address this, each Mie image was normalized to make the energy of the laser sheet constant spatially. Minimum and maximum thresholds were set to eliminate background noise, reflections from the chamber, and secondary Mie scattered light from out of plane spray. Once processed, similar techniques to Schlieren were employed to binarize the spray image and detect edges of the individual plume, i.e., the front plume (left as seen in Figure 3d). It was also observed that the laser sheet attenuates as it propagates through the chamber perpendicular to the axis of injection, due to the presence of spray. This, however, did not have an impact on the measurements, as the front edge of the spray was free of this aberration and hence, was used for valuable quantitative measurements. Three iterations of each test condition were performed for all time instances. Once the front edge was defined, the corresponding pixels were calibrated, averaged over three iterations, and then plotted to obtain maximum liquid penetration lengths as a function of time.

FIGURE 3 (a) Schematic of the top-view of planar Mie scattering imaging setup, (b) Spray-G injector alignment relative to the laser sheet bisecting the front and back nozzles, (c) isometric 3-D rendering of HPSC and Mie laser sheet, and (d) schematic of corresponding Mie image with illuminated liquid spray plumes in the plane of the laser sheet, and associated nomenclature.

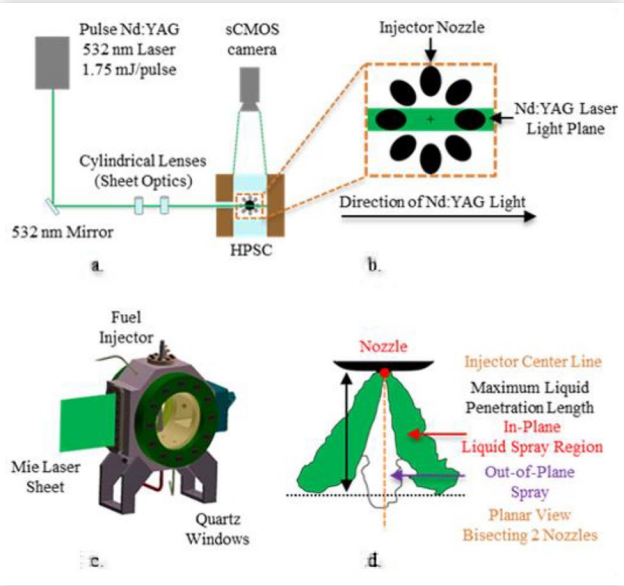

Test Conditions

Table 1 includes an array of test conditions specified by ECN that have been tested in prior literature and are standards within the ECN community [10, 31, 35-37]. These test conditions are denoted as G2, G2C, G3, and G3C. G2 conditions are representative of an early injection event creating a homogonous mixture, whereas, G3 conditions represent part-load, throttled, early injection conditions in a DI engine cylinder. Iso-octane and propane are widely used as surrogates for gasoline and LPG fuels, respectively [10, 27, 38]. As many studies have explored the spray morphology and mixing processes of iso-octane using the ECN Spray G fuel injector, iso-octane was also used to verify the experimental setup [29, 30, 39].

Numerical Spray Simulations

The simulation campaign was carried out with the commercial CFD software CONVERGE (v3.0) [40]. The injection was modeled with a two-tiered approach: first, the simulation of the two-phase internal nozzle flow was carried out to provide insight into the trends in the mass flow rates and the initial

TABLE 1 Test matrix including Engine Combustion Network's identified experimental conditions.

	Test Conditions			
Control Parameter	**G2C**	**G2**	**G3C**	**G3**
Fuel	Iso-octane and Propane			
Injector	Spray G - 8-hole Axisymmetric			
Electric Injection Duration [µsec]	680			
Actual Injection Duration [µsec]	870			
Ambient Temperature (T_{amb}) [K]	293	333	293	333
Fuel Temperature (T_{fuel}) [K]	293	363	293	363
Ambient Pressure (P_{amb}) [Bar(a)]	0.5	0.5	1	1
Injection Pressure (P_{inj}) [Bar(g)]	200			

development of the spray plumes for each fuel; then, the results were used to inform the Lagrangian parcel spray model, which was then implemented to simulate the full HPSC domain.

Both the steps in the simulation campaign were carried out by discretizing the transport equations with spatial second-order accuracy and Euler implicit scheme for the time integration. The velocity-pressure coupling was realized through the pressure implicit with splitting of operators (PISO) method. The following two sections describe the details of the numerical simulation.

Nozzle-Flow Simulation Setup

The first step taken follows the approach described in the author's previous work [41] to characterize the fuel jet dynamics produced by the nozzles. The nominal geometry of the injector defines the computational system, which was mated with a hemispheric open-outlet boundary, as shown in Figure 4a. In the resulting domain, the multi-phase flow was handled with a single-fluid mixture model, considering that the relative velocity between the phases was in local equilibrium. With this assumption, a single set of transport equations - mass, momentum, total energy, and species - was solved based on the barycentric velocity of the mixture. The different phases were treated as species - liquid, gas, and fuel vapor - in a multi-component mixture, and the phase change was handled through source terms in the species equation. The magnitude of the source terms was determined with the homogeneous relaxation model (HRM) [25], which assumes that the local and instantaneous vapor quality evolves towards its equilibrium value according to a linear trend, based on a characteristic time scale. The characteristic time scale depends on the properties of the fluids and the local pressure and void fraction values, and its magnitude was determined according to an empirically obtained constant. According to previous results [42], the value of the constant allows to modify the speed of the phase-change, and the behavior of the spray in the near nozzle region. The grid was obtained via the cut-cell method with a base mesh of 240 µm, and it was refined to 15 µm in the regions of interest as shown by the center-plane of the injector reported in Figure 4b. The dynamic grid refinement to track the plume evolution in the open chamber was obtained via adaptive mesh refinement based on the second derivative of the velocity and species mass fraction.

For both iso-octane and propane, the needle motion was prescribed according to the X-ray measurement by Sforzo et al. [24], collected for different fuel at previously defined ECN's G2 conditions [31], initializing the motion from a minimum gap of 6.6 µm, according to the setup proposed by Yue [43]. The turbulence was modeled with a large eddy simulation (LES) approach, using the dynamic structure model.

Lagrangian Spray Simulation Setup The simulation of the spray in the HPSC was obtained with the Lagrangian-Eulerian method and the liquid phase was modeled according to the discrete droplet model [11]. The geometry of the chamber was discretized with the Cartesian cut-cell method (Figure 5a), defining a base grid size of 1.6 mm, and relying on adaptive-mesh refinement (AMR) to refine the cells according to the second derivative of velocity and fuel vapor mass fraction, as shown in Figure 5b for 500 µs ASI. The transport equations were defined according to the unsteady Reynolds-average (URANS) framework, and the k-ε RNG was chosen for the turbulence modeling. The Lagrangian spray sub-models involve: Kelvin Helmotz Rayleigh Taylor (KH-RT) model [44] for primary and secondary break-up without the definition of a breakup length, Frössling correlation for phase-change, O'Rourke model [45] to introduce turbulent perturbation, and no-time-counter model [46] for droplet collision and coalescence. Moreover, to introduce the phase-change due to flash-boiling, the model proposed by Adachi et al. [26] is implemented in the code. This model accounts for local and instantaneous super-heat degree of the fuel in the chamber in terms of difference between the local temperature at the saturation temperature of the fuel at the local pressure. The implementation in CONVERGE is reported in previous work by the authors [47]. The spray parcels were initialized with the blob-injector model, which was informed with the results obtained by the nozzle-flow simulation in terms of mass flow rate and droplet momentum, plume direction, and plume angle to best represent the ensuing spray.

FIGURE 4 (a) Eulerian nozzle flow CFD domain for the ECN's Spray-G injector, and (b) numerical grid on the centerline at full needle lift.

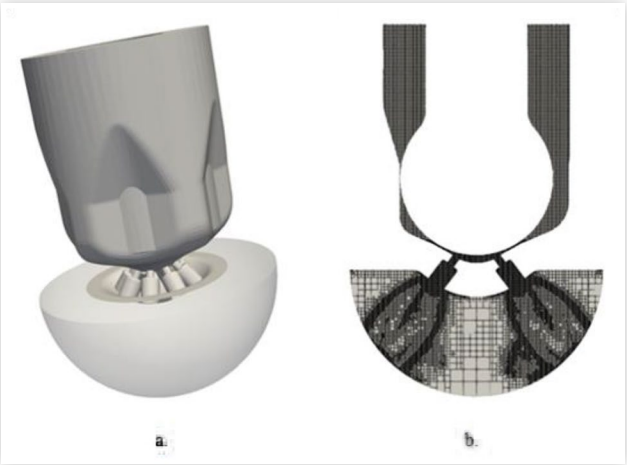

FIGURE 5 Lagrangian spray CFD domain for the injection in HPSC (a), and (b) numerical grid on the centerline with AMR.

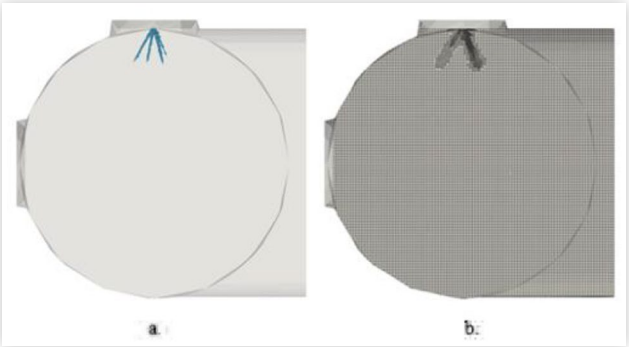

Numerical Spray Processing

Given the unconventional propane spray behavior, where vaporization and collapse play a major role, the numerical spray results were processed to reproduce experimental Schlieren and Mie scattering data. The two processing routines aim to describe the full spray morphology and the liquid phase development respectively.

The Schlieren images were reproduced by projecting the magnitude of the gradient of the gas-phase density along the line-of-sight, as shown in Figure 6a. The resulting 2D data was normalized on its maximum value to provide a qualitative image of the spray morphology as in Eq. 1.

$$I_{Sch,norm} = \frac{\sum_i^{cell\_X} grad_X(rho)}{\max\left(\sum_i^{cell\_X} grad_X(rho)\right)} \quad (1)$$

On the other hand, the light scattered from the liquid phase was reproduced by projecting over the line-of-sight, with the frontal area of the spray parcels projected over the thickness of a sampling region representative of the laser sheet, as shown in Figure 6b. Then, the obtained 2D projection of the spray parcel frontal area was normalized on its maximum value to produce a qualitative representation of measured scattered light, according to Eq. 2.

$$I_{norm} = \frac{\sum_i^{Nparcels} n\_drop_i D_i^2}{\max\left(\sum_i^{Nparcels} n\_drop_i D_i^2\right)} \quad (2)$$

The location and thickness of the sampling region replicates the experimental setup. The resulting images from both routines are proportional to the measured light intensity trends, but without implementing the laser scattering detailed dynamics, the focus of the validation is set on the boundaries of the spray profiles. To do so, the obtained light intensity profiles are binarized to highlight the fuel jet evolution in the chamber. The vapor penetration was determined by the maximum axial distance computed from binarized images generated with a threshold of $I_{Sch,norm} > 0.02$. The proposed comparison is chosen to allow the spray morphology assessment to be consistent with the experiments, and to enable the validated simulation to provide further insight on the vapor and liquid distribution trends.

FIGURE 6 Schematic of the spray simulation processing regions of interest: sampling region representing the (a) planar gradient density sampling of the gas phase to reproduce Schlieren data, and (b) the Mie laser sheet.

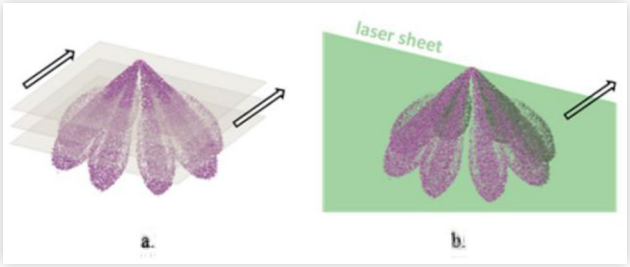

Results and Discussion

This section presents experimental and numerical measurements mapping out the spray morphology for iso-octane and propane over a range of engine-like conditions as mentioned above. The results from the experimental spray visualization techniques feed the numerical simulation results and aid in the validation and selection of a correct modeling technique, using a strong comparison of the qualitative and quantitative experimental results.

Experimental Spray Visualization Techniques Results

Experimental High-Speed Schlieren Results Figure 7 shows Schlieren imaging for iso-octane and propane at G3C and G3 conditions at three timesteps: 200 µs, 500 µs, and 750 µs ASI. As seen in Figure 7a-f, iso-octane has a wide injection angle, a typical spray pattern, and three individual plumes are clearly distinguishable. Majority of the spray appears to be symmetric at presented times

FIGURE 7 High-speed Schlieren images at various denoted timesteps (across) after the start of injection for various fuels and conditions (down), namely: (a) - (c) for iso-octane at G3C, (d) - (f) for iso-octane at G3, (g) - (i) for propane at G3C, and (j) - (l) for propane at G3 condition, respectively.

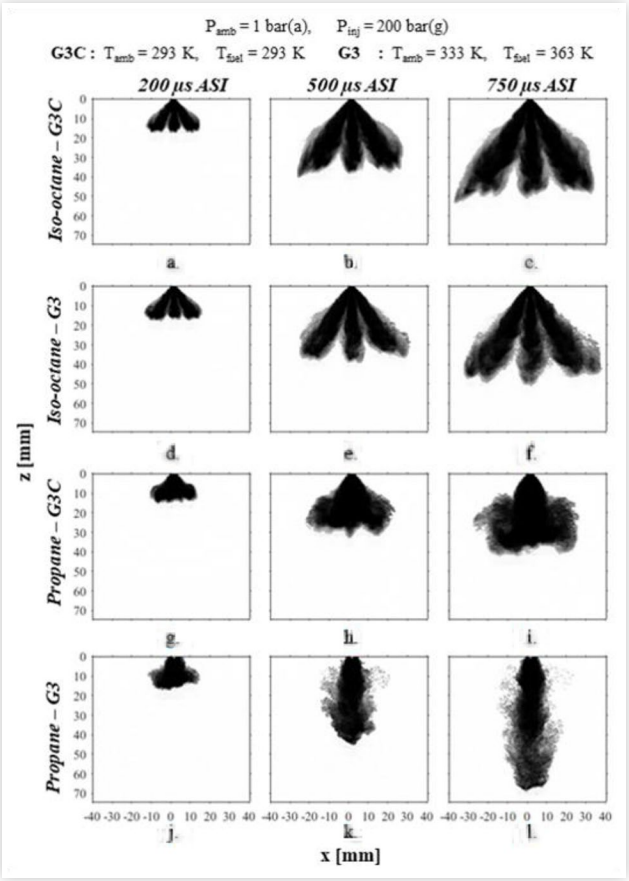

stamps for both conditions. It can be seen that the spray structure, penetration lengths and widths of iso-octane are minimally affected by the increasing temperature from G3C (T_{fuel} = T_{amb} = 20 °C) to G3 (T_{fuel} = 90 °C and T_{amb} = 60 °C). There is a clear distinction between darker/liquid spray cores and lighter/vapor regions for iso-octane.

Whereas propane in Figure 7g-l, has a much narrower overall injection angle and plume-to-plume interactions are prevalent creating a large singular jet. The spray structure of propane is observed to have a strong dependence on temperature. At colder cases (G2C and G3C), Figure 7g-i, the spray starts with a wide angle and less vaporization, but the multiple plumes of the spray collapse into a singular jet as it propagates through time. This influence of temperature increases in orders of magnitude when the fuel is preheated and injected into hotter ambient conditions (G2 and G3), as seen in Figure 7j-l. Contrary to the behavior observed in Figure 7g-i, propane's collapse is more evident at G3 conditions, seen in Figure 7j-l, as the width of the jet is narrower and stays consistent throughout the injection duration; propane also propagates further axially at hotter conditions. The axial penetration lengths of propane at G3 are much greater than iso-octane for all tested conditions. No clear distinction between liquid regions and vapor regions can be made for propane at both conditions.

The quantitative penetration measurements of iso-octane, agree strongly with the qualitative analysis presented. Penetration lengths and widths overlap well within the margin of experimental error throughout the injection duration, as seen in Figure 8a and b. Small deviation can be observed after the end of injection, i.e., 870 µs ASI, where differences in penetration lengths and widths start to appear and are within ± 7.5 mm. The penetration lengths increase in

the order of G3 < G2 ≈ G3C < G2C, i.e., penetration lengths are inversely proportional to temperature and pressure. However, when observing penetration widths, temperature has negligible effects, whereas the widths are inversely proportional to pressure after the end of injection. Iso-octane, as seen in Figure 8c, is observed to have a high velocity at higher temperatures towards the start of injection but decreases at a faster rate compared to colder temperatures, resulting in slower propagations at the end of injection.

Unlike iso-octane, propane has a clear trend for penetration lengths and the influences of various conditions. The axial penetration length, as observed in Figure 9a, is seen to be increasing for the conditions in the order of G3C < G2C < G3 < G2, i.e., inversely proportional to pressure and directly proportional to temperature. The direct proportionality with temperature is unique to propane. In general, propane is seen to propagate farther than iso-octane by approximately 20 mm more at 1200 µs. However, the penetration widths of propane, presented in Figure 9b, are significantly less as compared to iso-octane; approximately 50 mm less at 1200 µs. This agrees well with the qualitative images (Figure 7g-l) which show a narrower singular jet for propane. Not only the widths are smaller, but propane also shows an influence of temperature, not pressure which was seen in iso-octane. These features of a narrower, longer jet of propane also impact the penetration speeds plotted in Figure 9c, which are approximately 30 m/s higher than that of iso-octane. Hotter temperature conditions

FIGURE 8 Measurements for iso-octane including a) maximum axial vapor penetration length, b) maximum transverse vapor penetration width, and c) vapor penetration speed of iso-octane calculated using the time derivative of the maximum axial penetration length at corresponding conditions and timesteps measured using high-speed Schlieren imaging. Error bars are included at suitable timestamps for improved legibility. Mean error of ± 2.0 mm in vapor penetration lengths, ± 1.8 mm in vapor penetration widths, and ± 8.3 m/s in vapor speeds were observed over all tests for iso-octane.

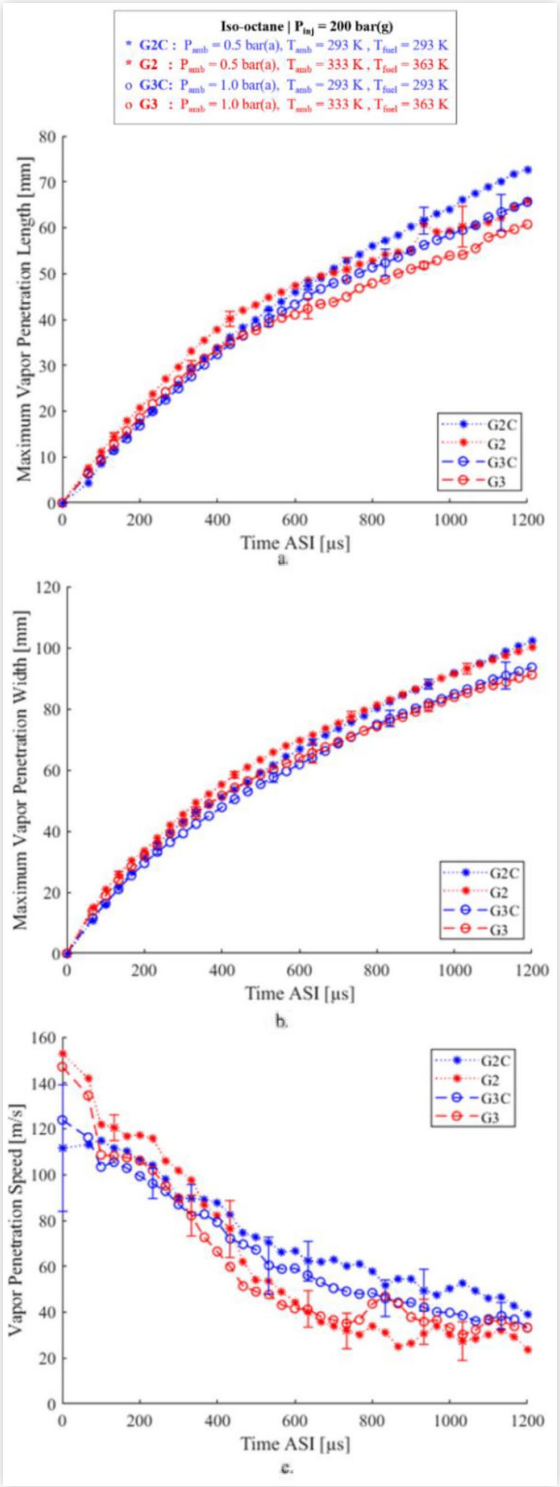

(G2 and G3) have a higher initial axial velocity than colder temperatures (G2C and G3C), and this trend is generally consistent through the duration of the spray. The unique features observed of the propane's vapor penetration velocity (Figure 9c) are a steep drop at 100 µs for each condition, and pulsating velocities after.

Experimental Planar Mie Scattering Results Planar Mie scattering enhances the liquid regions of a singular spray plume which provides finer resolution of the spray morphology. Figure 10 shows planer Mie imaging of iso-octane and propane at G3C and G3 conditions at three timesteps: 200 µs, 500 µs, and 750 µs ASI. As seen in Figure 10a-f, a singular plume of iso-octane is observed that has wide injection angle relative to the nominal axis of injection, i.e., vertical, and a distinct narrow liquid core for the front plume. It is also important to note that only one plume is seen in the plane of the laser sheet; this corresponds to the aforementioned effect of laser attenuation.

It is observed that the liquid penetration length is influenced by the temperature difference in G3C and G3 conditions, however, the injection spray angle and horizontal spray penetration remain unaffected. These results from planar Mie agree strongly with the results obtained for iso-octane using Schlieren imaging (Figure 7a-f). Figures 10g-i and 10j-10l, present planer Mie scattering imaging for propane at G3C and G3 conditions, respectively. Unlike iso-octane, propane in most presented cases is observed as a singular jet. This jet is unlike the singular front plume observed for iso-octane and is seen to be brighter, longer, more axial, and with a wider liquid core. This, however, is not true for propane at G3C conditions, as seen in Figure 10g, a singular liquid spray plume is observed, similar to iso-octane. But, as the spray progresses, shown in Figure 10h and i, the spray structure begins to resemble a large singular spray jet, similar to that seen in the Schlieren imaging. At hotter G3 conditions, the liquid penetration length of propane is also observed to be much longer than that at colder temperature conditions. The penetration length of propane is also observed to be longer than that of iso-octane for all tested conditions.

For iso-octane, as seen in Figure 11a, the liquid penetration lengths for all conditions overlap until 400 µs ASI, with minor deviations approaching the end of injection. However, for hotter conditions (G2 and G3), liquid penetration lengths begin to fall around 800 µs and become zero at 1200 µs. This shows that temperature is inversely proportional to liquid penetration lengths for iso-octane but, only for spray propagation after the end of injection.

Unlike iso-octane, propane has a clear trend for penetration lengths and the influences of various conditions. The liquid penetration length is seen to be increasing for conditions in the order of G3C < G2C < G3 < G2, which is inversely proportional to pressure and directly proportional to temperature. This trend is identical for vapor penetration of propane as observed in Schlieren imaging. Similar to iso-octane, at hotter temperature conditions, propane's liquid penetration length, as seen in Figure 11b, begins to fall sharply at 1000 µs, while at colder temperature conditions (G2C and G3C) the penetration lengths continue to increase. At colder conditions, liquid propane is seen to propagate farther than liquid

FIGURE 9 Measurements for propane including a) maximum axial vapor penetration length, b) maximum transverse vapor penetration width, and c) vapor penetration speed of propane calculated using the time derivative of the maximum axial penetration length at corresponding conditions and timesteps measured using high-speed Schlieren imaging. Error bars are included at suitable timestamps for improved legibility. Mean error of ± 1.5 mm in vapor penetration lengths, ± 2.4 mm in vapor penetration widths, and ± 8.6 m/s in vapor speeds were observed over all tests for propane.

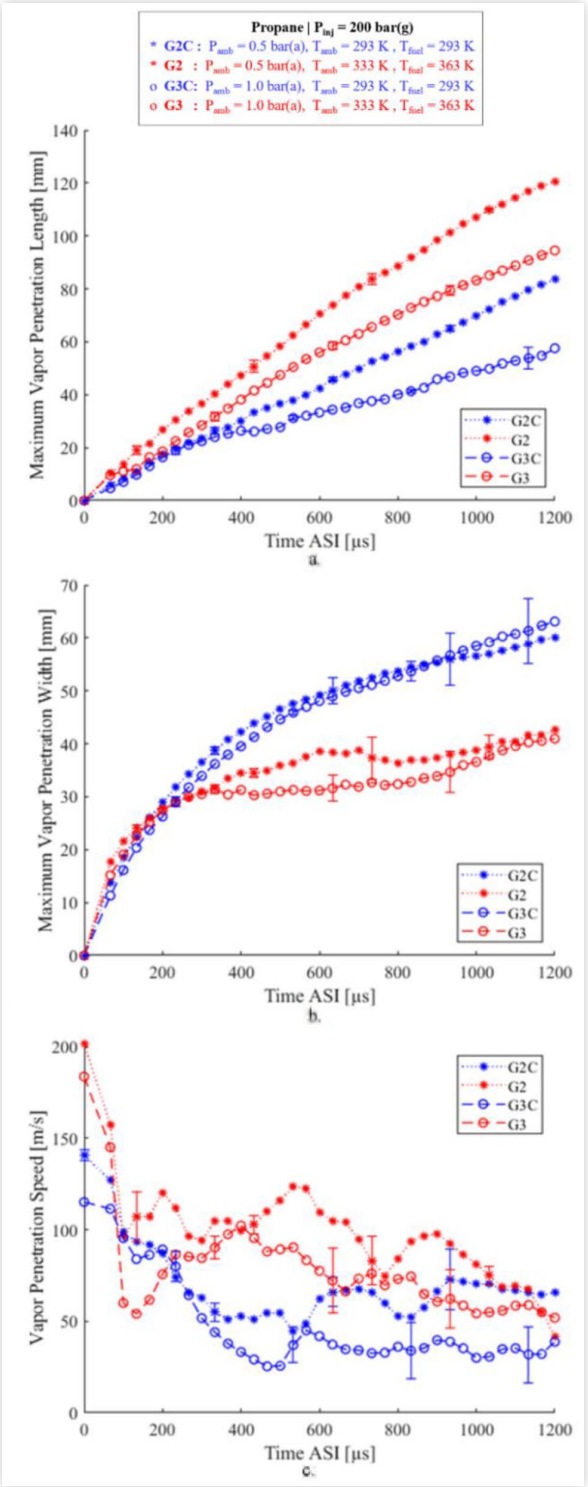

FIGURE 10 Planar Mie scattering images at various denoted timesteps (across) after the start of injection for various fuels and conditions (down), namely: (a) - (c) for iso-octane at G3C, (d) - (f) for iso-octane at G3, (g) - (i) for propane at G3C, and (j) - (l) for propane at G3 condition, respectively.

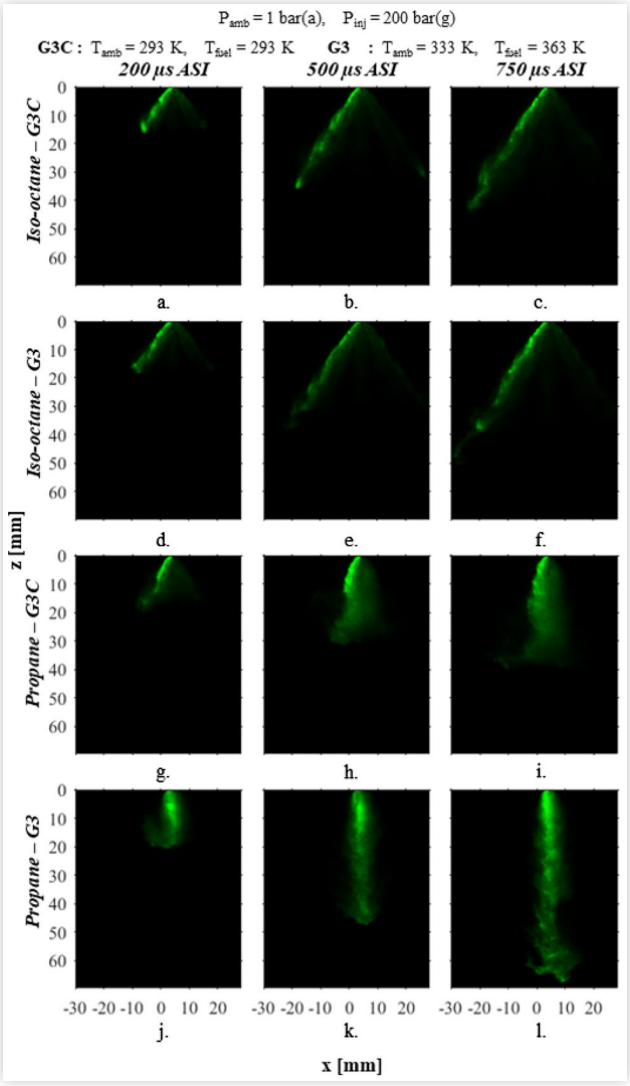

iso-octane by approximately 15 mm more at 1200 µs, however, at hotter conditions no liquid is observed for both fuels at 1200 µs.

Both vapor and liquid penetration lengths are crucial measurements that define the spray morphology and provide useful information describing how the spray propagates through time. Figure 12a and b present iso-octane and propane's vapor and liquid penetration lengths respectively, plotted at G3C and G3 conditions for a comparative analysis. For both the conditions, it is observed in Figure 12a that for iso-octane, the vapor leads the liquid by a small margin for the entire spray duration. However, for G3 condition, i.e., the hotter case, the liquid starts to fall significantly after the end of injection, causing the liquid-vapor difference to increase sharply. Unlike iso-octane, a clear distinction can be made between the penetrations for hot and cold conditions for

FIGURE 11 Maximum axial liquid penetration length measurements for a) iso-octane, and b) propane at corresponding conditions and timesteps measured using planar Mie Scattering imaging. Error bars are included at tested timestamps with a mean error in liquid penetration lengths of ± 2.8 mm for iso-octane, ± 1.8 mm for propane. A strong directly proportional relationship of the increased error and duration after start of injection was observed for both tested fuels.

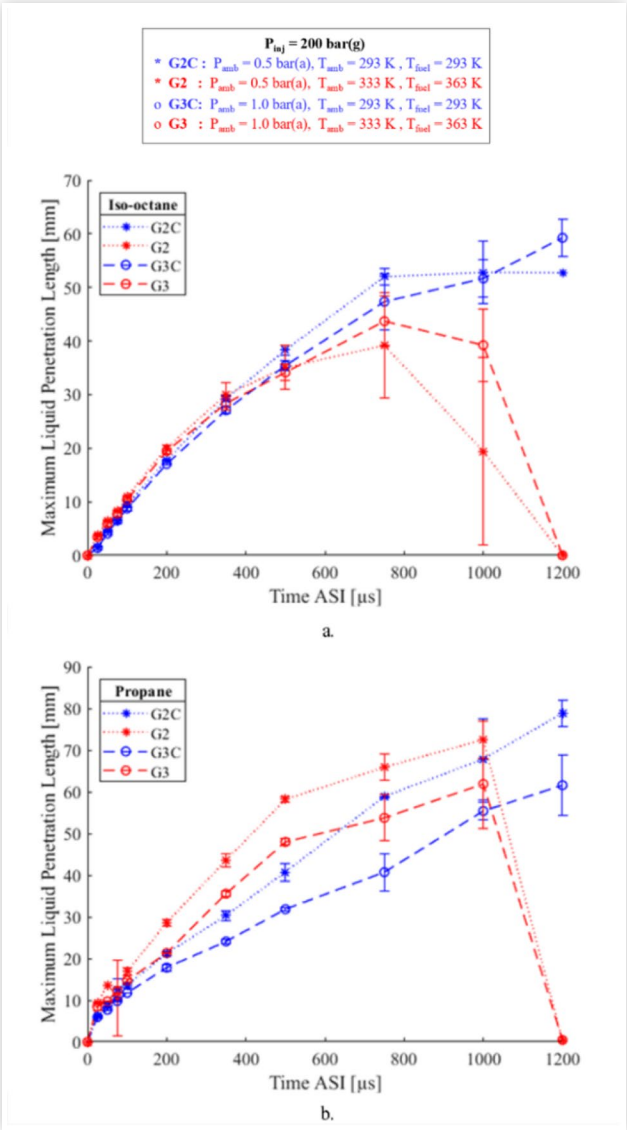

propane, as observed in Figure 12b. For G3C conditions, liquid and vapor mostly overlap for the entirety of the spray propagation, however, the penetration length for the cold case is less than the hotter case, about 40 mm shorter at 1200 µs. Unlike the overlap as seen in G3C, G3 shows a steep drop in liquid penetration after the end of injection, leading to vapor penetrating to 90 mm and no liquid at 1200 µs.

As seen for both Schlieren and Mie imaging, crucial information from vapor and liquid penetration length, width, and speed measurements is used to define characteristics of the spray morphology. Iso-octane is minimally affected by

FIGURE 12 A comparison of maximum axial liquid vs. vapor penetration length for a) iso-octane, and b) propane at corresponding conditions and timesteps as a combined effort of high-speed Schlieren and planar Mie scattering imaging techniques. Error bars are included at suitable timestamps for improved legibility and comparison. The error ratios are same as observed in corresponding single phase experimental results.

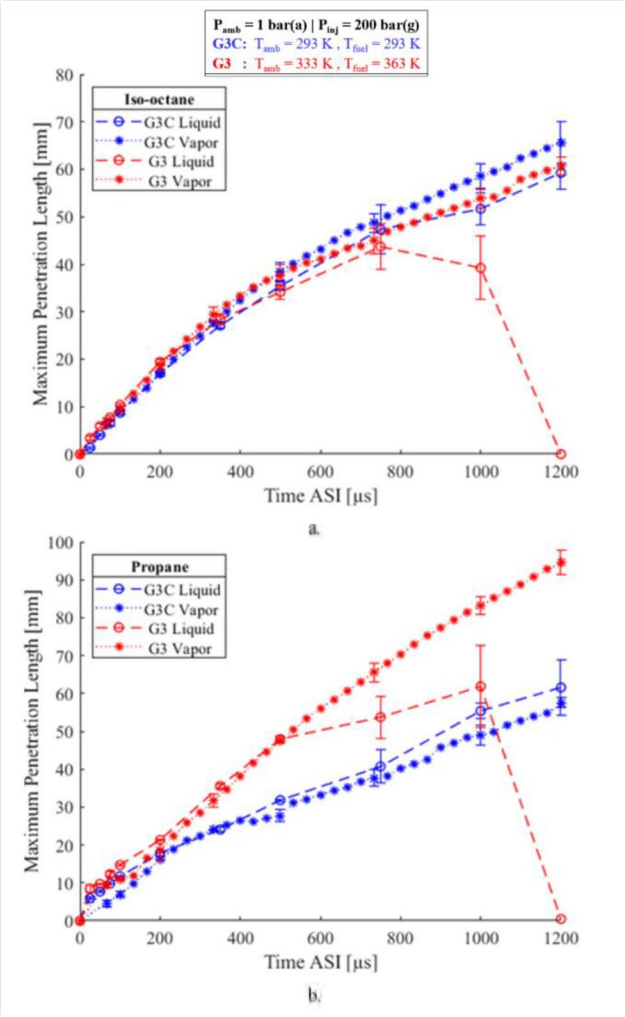

temperature and pressure as seen in the qualitative and quantitative analysis from Schlieren and Mie imaging. It is also observed that most of iso-octane's spray propagation is contributed by its liquid cores, i.e., insignificant difference between liquid and vapor penetration lengths. This is largely due to the physical characteristics of iso-octane, namely, low volatility, high viscosity, and higher density than compared to that of propane. These properties help prolong the existence of the liquid phase of the fuel and produce a conventional spray pattern in iso-octane, i.e., wider spray angles and distinct plumes as observed in Figures 7a-f and 10a-f, leading to a homogenous mixture both axially and transversely throughout the HPSC for all tested conditions. The observation of distinct plumes can be inferred to the absence of flash boiling effects in iso-octane, due to its low volatility, and high viscosity. A clear and consistent relationship between vapor and liquid penetration of iso-octane can also be observed by comparing Schlieren with planar Mie. Since iso-octane's spray does not experience severe flash boiling and collapse, the amount of liquid injected in the plane of the Mie laser sheet is only contributed by one plume of the 8-hole injector; therefore, decreasing the scattered laser intensity, and causing iso-octane to appear dimmer than propane in Mie images presented in Figure 10.

Unlike iso-octane, propane, due to its high volatility and low viscosity, experiences severe flash boiling at all tested conditions. This greatly impacts the spray morphology, structure, and mixing processes of the fuel. As seen in Schlieren imaging (Figure 7g-l), all of the eight individual plumes collapse into a singular jet due to its high super-heat degree. Propane at colder conditions appears to have wider spray angles, minimal collapse, and some plume-to-plume distinction, whereas these features are completely absent at hotter conditions, signifying that the magnitude of super-heat degree of propane is strongly dependent on temperature. This also impacts the mixing processes of propane, as it transitions from semi-axially dependent mixing at colder conditions to strongly axially dependent mixing at hotter conditions. Another key feature to note about propane, contrary to iso-octane, is that at the tested conditions, the majority of propane's spray propagation is fed by its flash boiling, spray collapse, and high degree of vaporization. This also explains the direct proportionality of propane's penetration length with temperature. When comparing Mie images, propane's jet appears to be brighter compared to iso-octane's singular plume; this can be misleading as it might signify presence of more liquid in the cases of propane. However, it is worth noting that the collected Mie images in Figure 10 are for planar Mie, not global Mie, and unlike iso-octane where only one nozzle of the injector is contributing to the liquid concentration inside the laser plane, for propane, multiple nozzles collapse and contribute to its liquid concentration within the plane making it appear brighter. From Schlieren measurements in Figure 9c, it was also observed that propane's velocity pulsated after the first 100 µs for all conditions, this effect was only seen in propane and can be attributed to the presence of shock structures within the fuel jet and gas-like injection of propane. All these unique features of propane and its variation from iso-octane's spray pattern, contribute to its classification as an unconventional spray.

Numerical Spray Simulation Results

The first step of the simulation campaign is to simulate nozzle flow to provide quasi-steady mass flow rate values that are to be imported in the initialization of the Lagrangian spray. Previous results [41] for iso-octane operated at P_{inj} = 200 bar and T_{fuel} = 363 K are compared with the values obtained in the G3C and G3 conditions, to scale the injection rate of the spray. Figure 13 shows the comparison between the different quasi-steady mass flow rates, which result 12.0% and 13.4% lower than iso-octane, for propane at G3C and G3 conditions, respectively.

FIGURE 13 Comparison of the mass flow rate at quasi-steady needle lift operation for iso-octane at G3 (black) injection conditions, G3C (blue), and G3C (red) for propane.

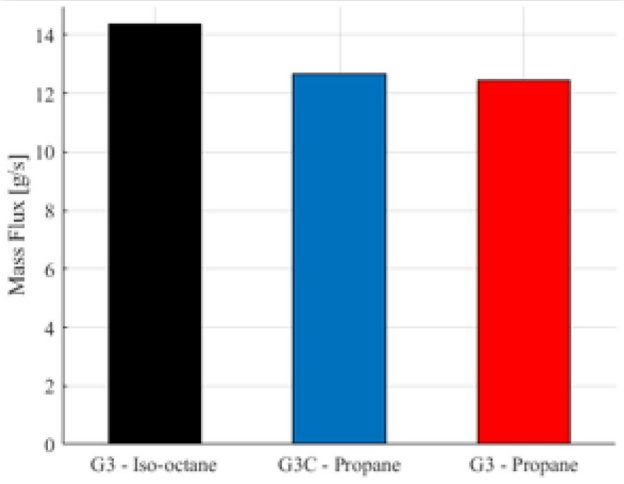

FIGURE 14 Mixture density profiles at quasi-steady injection condition for the injection of propane at (a) G3C, and (b) G3 conditions.

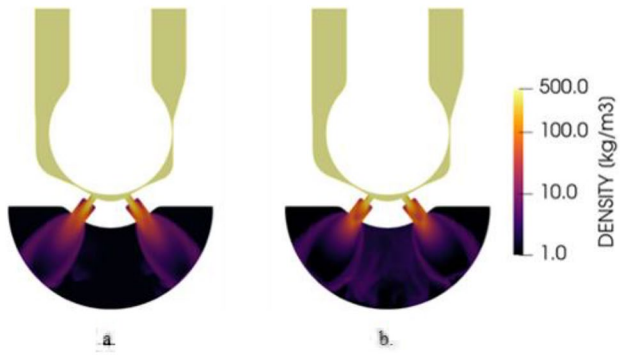

Moreover, the results from the nozzle flow simulation are used to guide the selection of the propane spray plumes entering the chamber, in terms of plume angle, which results in significantly higher values than experienced by GDI spray. In presence of an under-expanded jet, the rigorous calculation of a spray cone-angle in the near nozzle region is not trivial. The selection of the input for the Lagrangian spray parcels is therefore based on a sensitivity study on cone angles ranging from the standard gasoline reported by Payri [21] to 40°, which can reproduce the sudden expansion of the jet, clearly shown by the mixture density profile in Figure 14.

Due to the higher temperature of the fuel, G3 conditions show a higher initial expansion, observed in Figure 14b, which is driven by the higher super-heat degree of the fuel entering the chamber. This information is kept consistent in the setup of the Lagrangian spray.

Lagrangian Spray Simulation Results

The Lagrangian spray simulations in this work present preliminary results from an effort to define a computational framework capable of reproducing the behavior of propane sprays for engine-like conditions. The focus of this simulation campaign is to capture fuel development in the HPSC, which will be validated against optimal experimental measurements. Three conditions have been simulated: (i) G3 with iso-octane, (ii) G3C with propane, and (iii) G3 with propane. As stated in the section describing the numerical simulation processing methods, the results are qualitatively compared with experimental results from the HPSC obtained through Schlieren and Mie scattering imaging techniques. The numerical results are compared with the experimental data in terms of spray morphology and axial penetration. The setup for the injection of iso-octane at G3 conditions is based on the previous work by the authors [47] and re-processed to replicate Schlieren and Mie scattering images. The injection of propane at G3C and G3 conditions implement the same flow rate profile, which is scaled on the simulated mass flows obtained from the nozzle-flow simulations as shown in Figure 13.

Preliminary studies on the mesh resolution reported that a minimum cell size of 0.2 mm, obtained through adaptive mesh refinement, was able to generate results comparable to the experiments with CPU-times compatible to engine simulations. The representation of the vaporization-driven collapse of the plumes is achieved by enlarging the initial cone angle (C_A) of the blob injector to 40° and keeping the inclusion angle (I_A) consistent with the nominal direction of the nozzles equal to 37°; with the cone angle controlling the angle of the spread of the injectant and the inclusion angle being defined as the deviation from the injector axis for a single nozzle. Both of these variables produce an effect on the axial penetration and the morphology of the spray, as well as potentially influencing the spray breakup and atomization for different conditions. The simulation results for propane were found to be sensitive to both the I_A and the nominal direction of the nozzles; to illustrate this sensitivity, spray morphology comparisons are shown for a range of C_A, as well as I_A, for both G3C and G3 conditions in Figures 15 and 16, respectively. Numerical results are shown in Figures 15-18 at 750 µs ASI, as this timestep corresponds to maximum axial penetration and is the time at which differences between setups are most apparent. Additional timesteps were also compared with experimental results, and each simulation was performed from 0 to 1200 µs ASI.

The results in Figures 15 and 16 illustrate the influence of C_A and I_A on the spray morphology; namely, spray collapse is promoted as C_A is increased. This can be seen clearly at the lower I_A shown in Figures 15e and 16e. Whereas the effect of a higher I_A is seen as dissipation in the initial axial momentum component, thus reducing the maximum axial penetration, as observed in Figures 15f and 16f. The noticeable differences in spray morphology can be addressed by further examining the breakup model. Comparing the simulations results with experimental Schlieren vapor penetration lengths and widths, I_A of 37° and C_A of 40° were found to model the penetration profile accurately for injection of propane at both G3C and G3 conditions. The final geometry modeling decisions made for the blob injector at G3C and G3 conditions are shown in Figures 15f and 16f, respectively

Improvements can be made in capturing the spray morphology by considering the KH model breakup time and model size constant for the Rayleigh-Taylor (RT) model [48].

FIGURE 15 Projected density gradient of the gas phase from Lagrangian spray simulations (simulated Schlieren) of injection of propane at G3C conditions modeled for variations in cone angle C_A (down) and inclusion angle I_A (across). Final geometry modeling decisions made for G3C conditions shown in (f).

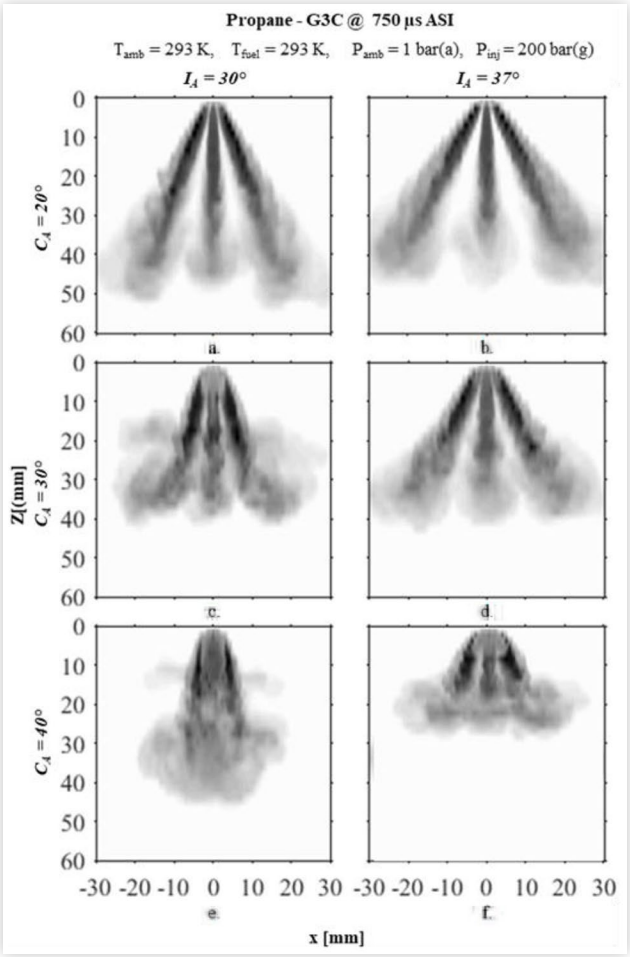

FIGURE 16 Projected density gradient of the gas phase from Lagrangian spray simulations (simulated Schlieren) of injection of propane at G3 conditions modeled for variations in cone angle C_A (down) and inclusion angle I_A (across). Final geometry modeling decisions made for G3 conditions shown in (f).

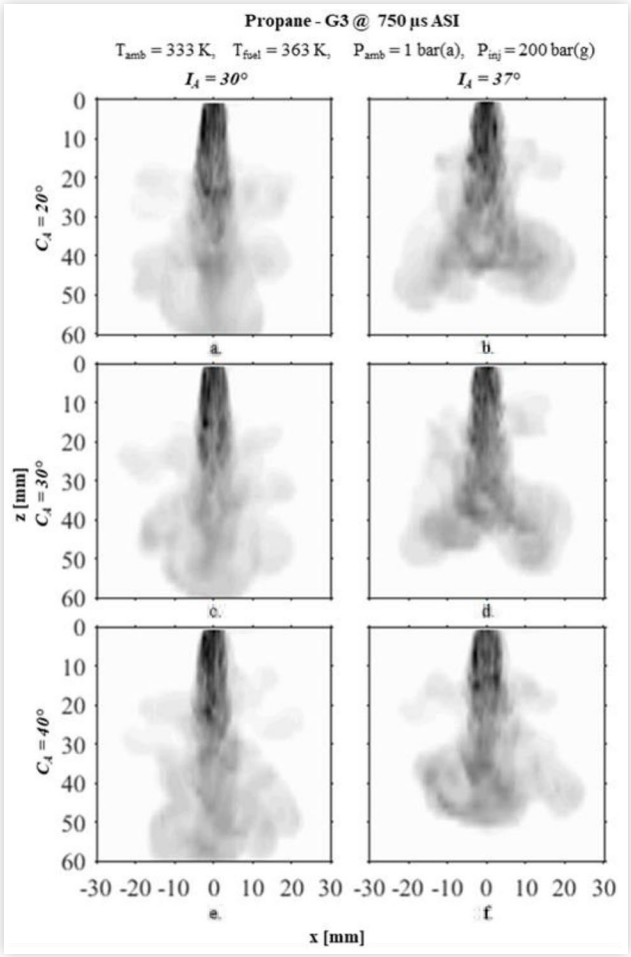

Extreme flashing conditions are simulated by decreasing the model breakup time constant from 1.0 (corresponding to non-extreme flashing conditions) to 0.1, and by decreasing the model size constant from 0.6 (corresponding to non-extreme flashing conditions) to 0.25. In particular, two conditions were simulated: (i) parameters corresponding to conditions without extreme flashing, and (ii) with extreme flashing. Results for propane injection at G3C conditions can be seen in Figure 17, with results for propane injection at G3 conditions shown in Figure 18. It was observed that at G3 conditions, accounting for extreme flashing improved the spray morphology in terms of comparison with experimental results seen in Figure 18a. It was found that at G3C conditions, improvement in terms of comparable morphology of the Lagrangian spray with experimental results was achieved for parameters corresponding to non-extreme flashing conditions, most notably in the spray collapse and in the maximum spray penetration. For the different conditions simulated, the chosen setup is given by Figure 17b for G3C, and Figure 18c for G3. The differences in modeling parameters are due to the different spray morphologies observed for the two conditions simulated. The

FIGURE 17 (a) Experimental Schlieren image of propane at G3C; projected density gradient of the gas phase from Lagrangian spray simulations (simulated Schlieren) of injection of propane at G3C conditions modeled with Rayleigh-Taylor breakup time and model size constants corresponding to (b) non-extreme flashing conditions, and (c) extreme flashing conditions. Final modeling decisions made for G3C conditions shown in (b).

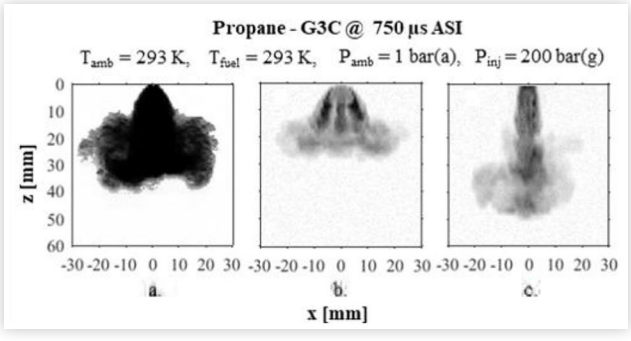

FIGURE 18 (a) Experimental Schlieren image of propane at G3; projected density gradient of the gas phase from Lagrangian spray simulations (simulated Schlieren) of injection of propane at G3 conditions modeled with Rayleigh-Taylor breakup time and model size constants corresponding to (b) non-extreme flashing conditions, and (c) extreme flashing conditions. Final modeling decisions made for G3 conditions shown in (c).

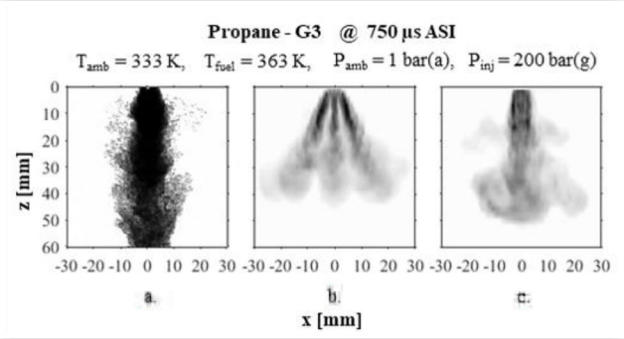

FIGURE 19 Projected density gradient of the gas phase from Lagrangian spray simulations (simulated Schlieren) of injection of (a) iso-octane at G3, (b) propane at G3C, and (c) propane at G3 condition at denoted timestamps.

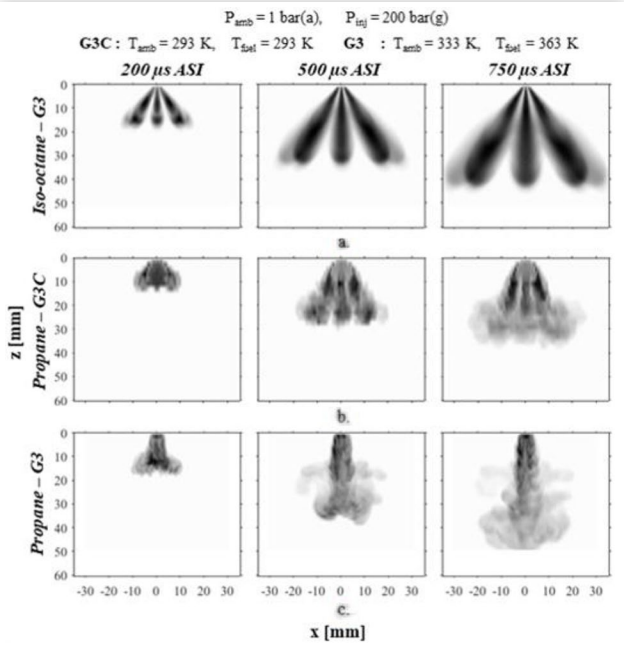

model breakup effect is quite strong for higher temperatures; for G3 conditions it is necessary to account for rapid vaporization of small droplets, and modeling parameters corresponding to extreme flashing, to capture these effects. For lower temperature conditions, i.e., G3C, the vaporization rate is lower and does not drive morphology as severely, and the model breakup effect is less dominant.

The projected gradient of the gaseous phase density in the Eulerian domain, which includes both fuel vapor and ambient N_2, is reported in Figure 19 for the three different conditions at 200 µs ASI, 500 µs ASI and 750 µs ASI. The results highlight that the Lagrangian simulation can capture the fuel effect for the tested conditions. Propane shows strong plume-to-plume interaction and complete collapse of the spray around the injector axis for both G3C and G3. The higher penetration measured in G3 conditions is reproduced by the simulations. This behavior is directly correlated to the temperature of the fuel and its consequent vaporization propensity. When injected at ambient temperature - both for fuel and ambient, at G3C conditions - the vaporization rate of the fuel decreases due to the lower vapor pressure and the reduced thermal energy available in the chamber. The collapse is less abrupt, and the axial velocity of the resulting vapor jet is lower, generating a wider and shorter spray evolution.

Quantitatively, the results capture the fuel effect, but the vapor penetration shown in Figure 20, calculated from the maximum axial distance from the injector location where the normalized gradient is higher 0.02 with binarized images, is under predicted for propane injection at G3C and G3 conditions (Figure 20b). This discrepancy is ascribed to the lack of a dedicated flash-boiling model for the parcels and to the simplified injector model used for the propane injection. The blob injector model in fact assumes only liquid injection, with droplet sizes defined as a function of the nozzle diameter and of a discharge coefficient. These assumptions are not valid for an extremely volatile fuel like liquid propane at the tested conditions.

This lack of accuracy in the simulation is visible in the comparison with the Mie scattering results which highlight that the phase-change trend is not consistent with the experiments as shown in Figure 21. It is possible to notice that at a low-vaporization condition - iso-octane at G3 conditions - the penetration of the liquid parcels is strongly correlated with the density gradients in the gas phase reported in Figure 19. For propane, and especially for the most superheated conditions - G3 - the vaporization is almost instantaneous and differs from the collapse spray core seen experimentally. These results underline the lack of accuracy of the Lagrangian spray models in representing extremely vaporizing sprays.

The current work represents a first assessment of the capability of the commonly available models for engine-spray simulations and highlight the fact that, despite the reasonable agreement obtained in the fuel vapor morphology, the representation of the liquid phase lacks accuracy. The addition of the flash-boiling vaporization terms on the phase-change modeling further reduces the liquid penetration without improving the representation of the vapor dynamics. For propane, both G3C and G3 conditions, are extreme flashing conditions: the super heat degree, defined as P_{amb}/P_{sat} (T_{fuel}), is respectively 0.12 and 0.03, and the empirical correlation tends to over-estimate the phase-change.

Conclusions

In this study, iso-octane and propane, serving as surrogates for gasoline and LPG, were experimentally tested and computationally simulated for direct injections at a wide range of conditions corresponding to early injection, and part load,

FIGURE 20 Comparison between the experimental results of maximum axial vapor penetration of the spray from high-speed Schlieren imaging and computational results from projected density gradient of gas phase from Lagrangian spray simulations (simulated Schlieren) of (a) iso-octane at G3, and (b) propane at G3C and G3 conditions. Error bars are included at suitable timestamps in the experimental measurements for improved legibility and comparison. The error ratios are same as observed in corresponding single phase experimental results.

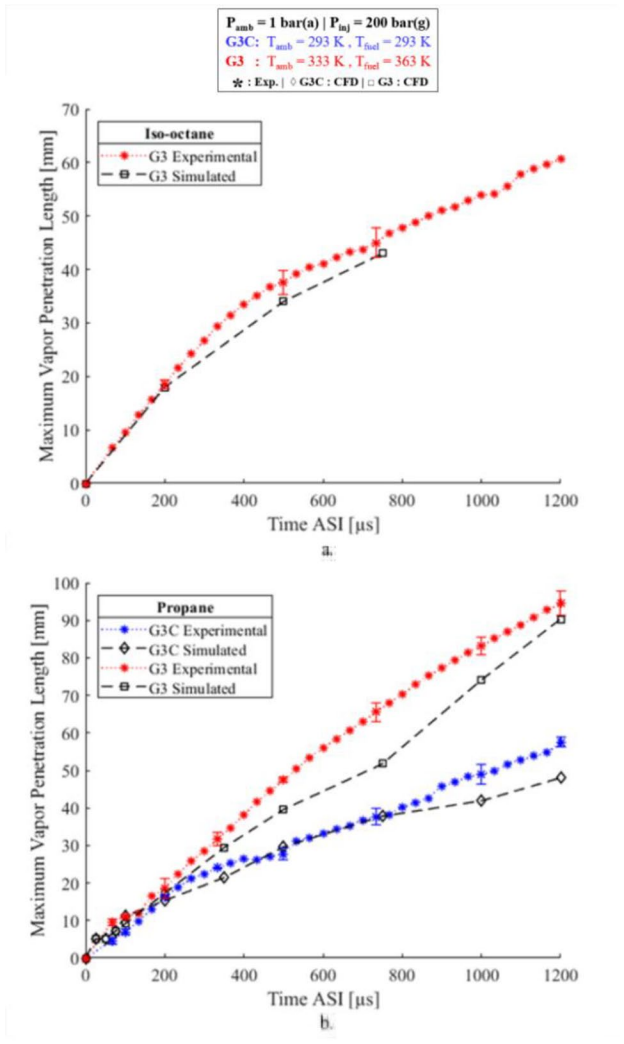

throttled conditions as seen in a direct injected spark ignited engine. These engine-like conditions were reproduced by controlling fuel and ambient temperatures and pressures, and the governing mechanisms of liquid and vaporous fuel sprays were examined in a quasi-quiescent, optically capable, HPSC. The results from the experimental spray diagnostics fed the numerical simulations for its model validation, selection, and tuning.

Optical imaging techniques revealed that iso-octane was minimally affected by temperature and pressure and exhibited a conventional spray pattern specifically, wider spray angles and explicit plume-to-plume distinctions. Iso-octane's penetration lengths were inversely proportional to both pressure

FIGURE 21 Projected density gradient over the line-of-sight of the liquid phase from Lagrangian spray simulations for the volume of the laser sheet (simulated planar Mie) of injection of (a) iso-octane at G3, (b) propane at G3C, and (c) propane at G3 conditions at denoted timestamps.

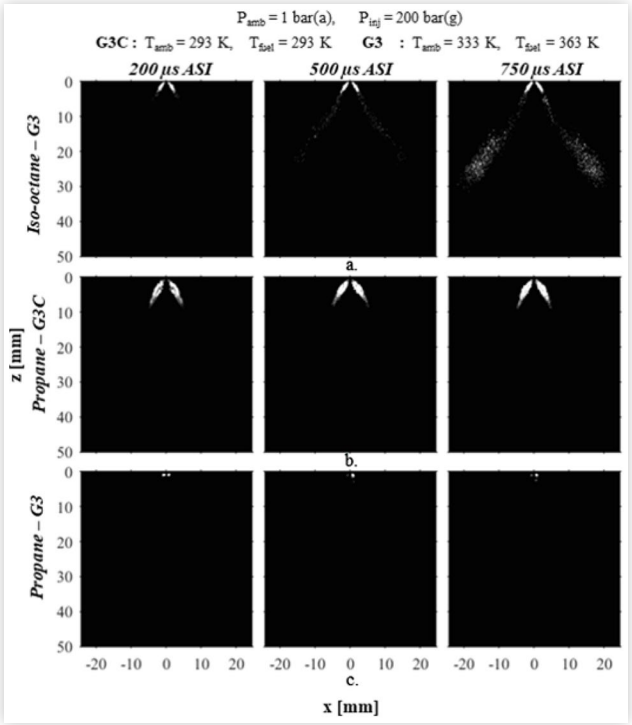

and temperature, and a similar trend on pressure dependence was observed for propane. Propane at colder conditions had wider spray angles, minimal collapse, and some plume-to-plume distinction, whereas these features were completely absent at hotter conditions, signifying the strong dependence of temperature or super-heat degree of propane on spray formation. Propane's spray propagation was fed by its flash boiling, spray collapse, and high degree of vaporization, resulting in a direct proportionality of propane's penetration length to temperature. These unique features of propane and its variation from iso-octane's spray pattern, contribute to its classification as an unconventional spray.

Best practices from standard gasoline direct injection models were imported in the framework and modified to capture the strongly collapsing propane spray dynamics. The simulations were based on a Lagrangian spray framework, and the characteristics of the injected droplets were modified according to higher-resolution multi-phase nozzle flow results. The simulation results were found to be sensitive to cone and inclusion angles of the blob injector, hence, the spray morphologies were mapped for various C_A and I_A, and the final selection was made by comparison with the experimental results. The current work represents a first assessment of the capability of the commonly available models for engine-spray simulations and highlight the fact that, despite the reasonable agreement obtained in the fuel vapor morphology, the representation of the liquid phase lacks accuracy. The addition of the flash-boiling vaporization terms on the phase-change modeling further reduces the liquid penetration without

improving the representation of the vapor dynamics. For propane, both G3C and G3 conditions, are extreme flashing conditions: the super heat degree, defined as P_{amb}/P_{sat} (T_{fuel}), is respectively 0.12 and 0.03, and the empirical correlation tends to over-estimate the phase-change.

Future Work

To enhance the distinction between vapor and liquid regions of propane, the current planar Mie scattering imaging will be coupled with planar laser induced fluorescence, carried out using acetone as a tracer, to increase resolution and obtain further insight into the mixing processes of propane. Higher ambient pressure conditions will also be incorporated into the data set, to explore the high load, homogonous charge, early injection and part load/idle, stratified charge, late injection conditions observed in DISI engines, for various commercially available GDI injectors, with and without modified nozzle geometries.

The simulation framework is currently being extended introducing more information from high-resolution nozzle flow simulations, such as vapor formation in the nozzle, estimation of the initial droplet size distribution, and detailed multi-phase flow momentum initialization. Ultimately the one-way coupling approach [49] will be implemented. Moreover, since flash-boiling dominates the dynamics of the spray, in terms of atomization and phase-change, detailed modeling of the phase-change will be addressed to predict the LPG and liquid propane injection. Finally, processing of the CFD results will be improved including the fuel dependency on the scattered light and possible dense fuel vapor effects to allow for more meaningful comparison to experimental data.

The efforts from the experimental and numerical spray campaign for LPG, will aid to identify an optimal DI nozzle geometry for homogonous and stratified charge mixture, and to find the ideal coupling between the in-cylinder motion, and timed injections events, using robust spray models to serve the overarching goal of achieving near diesel engine efficiency for a Cummins X-15 heavy-duty diesel engine using LPG.

References

1. Kim, K., Kim, J., Oh, S., Kim, C. et al., "Evaluation of Injection and Ignition Schemes for the Ultra-Lean Combustion Direct-Injection LPG Engine to Control Particulate Emissions," *Applied Energy* 194 (2017): 123-135, doi:10.1016/j.apenergy.2017.03.012.
2. "FACT SHEET: President Biden Sets 2030 Greenhouse Gas Pollution Reduction Target Aimed at Creating Good-Paying Union Jobs and Securing U.S. Leadership on Clean Energy Technologies | The White House," accessed December 2021, https://www.whitehouse.gov/briefing-room/statements-releases/2021/04/22/fact-sheet-president-biden-sets-2030-greenhouse-gas-pollution-reduction-target-aimed-at-creating-good-paying-union-jobs-and-securing-u-s-leadership-on-clean-energy-technologies/.
3. Jadun, P., McMillan, C., Steinberg, D., Muratori, M. et al., *Electrification Futures Study: End-Use Electric Technology Cost and Performance Projections through 2050* (Golden, CO: National Renewable Energy Laboratory, 2017), doi:10.2172/1416113
4. "Petroleum & Other Liquids - U.S. Energy Information Administration (EIA)," accessed December 2021, https://www.eia.gov/petroleum/index.php.
5. Morganti, K.J., Foong, T.M., Brear, M.J., da Silva, G., Yang, Y., and Dryer, F.L., "The Research and Motor Octane Numbers of Liquefied Petroleum Gas (LPG)," *Fuel*, vol. 108, pp. 797-811, 2013, doi: 10.1016/J.FUEL.2013.01.072.
6. "Alternative Fuels Data Center: Fuel Properties Comparison," accessed December 2021, https://afdc.energy.gov/fuels/properties.
7. "Alternative Fuels Data Center: Propane Basics," accessed December 2021, https://afdc.energy.gov/fuels/propane_basics.html.
8. Huang, Y., Hong, G., and Huang, R., "Investigation to Charge Cooling Effect and Combustion Characteristics of Ethanol Direct Injection in a Gasoline Port Injection Engine," *Applied Energy* 160 (2015): 244-254, doi:10.1016/j.apenergy.2015.09.059.
9. Kalam, M.A. and Masjuki, H.H., "An Experimental Investigation of High Performance Natural Gas Engine with Direct Injection," *Energy* 36, no. 5 (2011): 3563-3571, doi:10.1016/j.energy.2011.03.066.
10. Lacey, J., Poursadegh, F., Brear, M., Petersen, P. et al., "Optical Characterization of Propane at Representative Spark Ignition, Gasoline Direct Injection Conditions," SAE Technical Paper 2016-01-0842, 2016, https://doi.org/10.4271/2016-01-0842.
11. Dukowicz, J.K., "A Particle-Fluid Numerical Model for Liquid Sprays," *Journal of Computational Physics* 35, no. 2 (1980): 229-253, doi:10.1016/0021-9991(80)90087-X.
12. Lacey, J. et al., "Generalizing the Behavior of Flash-Boiling, Plume Interaction and Spray Collapse for Multi-Hole, Direct Injection," *Fuel* 200 (2017): 345-356, doi:10.1016/j.fuel.2017.03.057.
13. Guo, H., Nocivelli, L., Torelli, R., and Som, S., "Towards Understanding the Development and Characteristics of Under-Expanded Flash Boiling Jets," *International Journal of Multiphase Flow* 129 (2020): 103315, doi:10.1016/J.IJMULTIPHASEFLOW.2020.103315.
14. Nocivelli, L., Yan, J., Saha, K., Magnotti, G.M., et al. "Effect of Ambient Pressure on the Behavior of Single-Component Fuels in a Gasoline Multi-Hole Injector," in *ASME 2019 Internal Combustion Engine Division Fall Technical Conference, ICEF 2019*, December 2019, doi: 10.1115/ICEF2019-7258.
15. Price, C., Hamzehloo, A., Aleiferis, P., and Richardson, D., "Numerical Modelling of Droplet Breakup for Flash-Boiling Fuel Spray Predictions," *International Journal of Multiphase Flow*, vol. 125, p. 103183, Apr. 2020, doi: 10.1016/J.IJMULTIPHASEFLOW.2019.103183.
16. Lacey, J., Aditiya, H., Poursadegh, F., Brear, M. et al., "Flash Vaporization of Propane in an Optically Accessible, Directly Injected Engine," *International Journal of Engine Research* 22, no. 2 (2021): 685-696, doi:10.1177/1468087419849989.

17. Schlüßler, R., Gürtler, J., Czarske, J., and Fischer, A., "Planar Fuel Velocity Measurements in the Near-Nozzle Region of a High Pressure Diesel Injection Nozzle," in *18th International Symposium on the Application of Laser and Imaging Techniques to Fluid Mechanics*, 2016, pp. 1-13.
18. Melton, L.A., "Spectrally Separated Fluorescence Emissions for Diesel Fuel Droplets and Vapor," *Applied Optics* 22, no. 14 (1983): 2224-2226, doi:10.1364/AO.22.002224.
19. Ghandhi, J., Felton, P., Gajdeczko, B., and Bracco, F., "Investigation of the Fuel Distribution in a Two-Stroke Engine with an Air-Assisted Injector," SAE Technical Paper 940394, 1994, https://doi.org/10.4271/940394.
20. Fujimoto, H., Choi, D., Shima, Y., Senda, J. et al., "Two-Dimensional Imaging of Fuel-Vapour Concentration by Use of LIEF Technique during Mixture Formation Process in a DI Diesel Engine," *Measurement Science and Technology* 13, no. 3 (2002): 391, doi:10.1088/0957-0233/13/3/322.
21. Payri, R., Gimeno, J., Marti-Aldaravi, P., and Martínez, M., Nozzle Flow Simulation of GDi for Measuring Near-Field Spray Angle and Plume Direction," SAE Technical Paper 2019-01-0280, 2019, https://doi.org/10.4271/2019-01-0280.
22. Rogler, P., Grzeszik, R., Arndt, S., and Aigner, M., "3D Analysis of Vapor and Liquid Phase of GDI Injectors Using Laser Induced Exciplex Fluorescence Tomography in a High Pressure/High Temperature Spray Chamber," SAE Technical Paper 2007-01-1827 (2007). https://doi.org/10.4271/2007-01-1827.
23. Poursadegh, F., Lacey, J.S., Brear, M.J., and Gordon, R.L., "On the Phase and Structural Variability of Directly Injected Propane at Spark Ignition Engine Conditions," *Fuel* 222 (2018): 294-306, doi:10.1016/j.fuel.2018.02.137.
24. Sforzo, B.A. et al., "X-ray Characterization and Spray Measurements of ECN Spray G Using Alternative Fuels Under Flashing Conditions," *ILASS Americas* (2019).
25. Downar-Zapolski, P., Bilicki, Z., Bolle, L., and Franco, J., "The Non-Equilibrium Relaxation Model for One-Dimensional Flashing Liquid Flow," *International Journal of Multiphase Flow* 22, no. 3 (1996): 473-483, doi:10.1016/0301-9322(95)00078-X.
26. Adachi, M., McDonell, V.G., Tanaka, D., Senda, J. et al., "Characterization of Fuel Vapor Concentration Inside a Flash Boiling Spray," SAE Technical Paper 970871 (Feb. 1997), doi:10.4271/970871.
27. Mesman, P.H. and Veenhuizen, B., "The Spray Behavior of Liquid LPG at Different Back Pressures During Injection in a Constant Volume Chamber," SAE Technical Paper 2009-01-1834 (Jun. 2009), doi:10.4271/2009-01-1834.
28. Sforzo, B.A., Tekawade, A., Matusik, K.E., Kastengren, A.L. et al., "X-ray Characterization and Spray Measurements of ECN Spray G Using Alternative Fuels Under Flashing Conditions," *ILASS Americas* (2019).
29. Guo, H., Nocivelli, L., and Torelli, R., "Numerical Study on Spray Collapse Process of ECN Spray G Injector Under Flash Boiling Conditions," *Fuel* 290 (2021): 119961, doi:10.1016/j.fuel.2020.119961.
30. Allocca, L., Bartolucci, L., Cordiner, S., Lazzaro, M. et al., "ECN Spray G Injector: Assessment of Numerical Modeling Accuracy," SAE Technical Paper 2018-01-0306 (2018). https://doi.org/10.4271/2018-01-0306.
31. "Spray G Parametric Variation - Engine Combustion Network," *Engine Combustion Network*, accessed December 2021, https://ecn.sandia.gov/gasoline-spray-combustion/target-condition/spray-g-parametric-variation/.
32. Qi, Y.L., Xu, B.Y., and Cai, S.L., "An Application of Digital Image Processing Techniques to the Characterization of Liquid Petroleum Gas (LPG) Spray," *Measurement Science and Technology* 17, no. 12 (Nov. 2006): 3229, doi:10.1088/0957-0233/17/12/005.
33. Parrish, S.E., "Evaluation of Liquid and Vapor Penetration of Sprays from a Multi-Hole Gasoline Fuel Injector Operating under Engine-Like Conditions," *SAE International Journal of Engines* 7, no. 2 (2014): 1017-1033. https://www.jstor.org/stable/26277820.
34. Zeng, W., Xu, M., Zhang, M., Zhang, Y. et al., "Macroscopic Characteristics for Direct-Injection Multi-Hole Sprays Using Dimensionless Analysis," *Experimental Thermal and Fluid Science* 40 (2012): 81-92, doi:10.1016/j.expthermflusci.2012.02.003.
35. Mohan, B., Badra, J., Sim, J., and Im, H.G., "Coupled In-Nozzle Flow and Spray Simulation of Engine Combustion Network Spray-G Injector," *International Journal of Engine Research* 22, no. 9 (2021): 2982-2996, doi:10.1177/1468087420960612.
36. Hwang, J., Weiss, L., Karathanassis, I.K., Koukouvinis, P. et al., "Spatio-Temporal Identification of Plume Dynamics by 3D Computed Tomography Using Engine Combustion Network Spray G Injector and Various Fuels," *Fuel* 280 (2020): 118359, doi:10.1016/j.fuel.2020.118359.
37. Mohapatra, C.K. et al., "Collaborative Investigation of the Internal Flow and Near-Nozzle Flow of an Eight-Hole Gasoline Injector (Engine Combustion Network Spray G)," *International Journal of Engine Research* (2020), doi:10.1177/1468087420918449.
38. Sileghem, L., Alekseev, V., Vancoillie, J., Van Geem, K.M. et al., "Laminar Burning Velocity of Gasoline and the Gasoline Surrogate Components Iso-Octane, n-Heptane and Toluene," *Fuel* 112 (2013): 355-365, doi:10.1016/j.fuel.2013.05.049.
39. Montanaro, A., Allocca, L., and Lazzaro, M., "Iso-Octane Spray from a GDI Multi-Hole Injector under Non- and Flash Boiling Conditions," SAE Technical Paper 2017-01-2319, 2017, https://doi.org/10.4271/2017-01-2319..
40. Richards, K.J., Senecal, P.K., and Pomraning, E., *CONVERGE 3.0** (Madison, WI: Convergent Science, 2021)
41. Nocivelli, L., Sforzo, B., Tekawade, A., Yan, J. et al., "Analysis of the Spray Numerical Injection Modeling for Gasoline Applications," SAE Technical Paper 2020-01-0330 (2020). https://doi.org/10.4271/2020-01-0330.
42. Nocivelli, L., Zhang, A., Sforzo, B.A., Tekawade, A., et al., "Comparison Between a Center-Mounted and a Side-Mounted Injector for Gasoline Applications: A Computational Study," in *ASME 2020 Internal Combustion Engine Division Fall Technical Conference, ICEF 2020*, December 2020, doi: 10.1115/ICEF2020-2991.
43. Yue, Z., Battistoni, M., and Som, S., "Spray Characterization for Engine Combustion Network Spray G Injector Using High-Fidelity Simulation with Detailed Injector Geometry," *International Journal of Engine Research*, 2019, doi: 10.1177/1468087419872398.

44. Reitz, R.D. and Beale, J.C., "Modeling Spray Atomization with the Kelvin-Helmholtz/Rayleigh-Taylor Hybrid Model," *Atomization and Sprays* 9, no. 6 (1999): 623-650, doi:10.1615/atomizspr.v9.i6.40.
45. Richards, K., Senecal, P.K., and Pomraning, E., *CONVERGE 3.0 Manual* (Madison, WI: Convergent Science Inc., 2020)
46. Schmidt, D.P. and Rutland, C.J., "A New Droplet Collision Algorithm," *Journal of Computational Physics* 164, no. 1 (2000): 62-80, doi:10.1006/jcph.2000.6568.
47. Nocivelli, L., Yan, J., Saha, K., Magnotti, G.M., et al., "Effect of Ambient Pressure on the Behavior of Single-Component Fuels in a Gasoline Multi-Hole Injector," in *ASME 2019 Internal Combustion Engine Division Fall Technical Conference, ICEF 2019*, December 2019, doi: 10.1115/ICEF2019-7258.
48. Senecal, P., Richards, K., Pomraning, E., Yang, T. et al., "A New Parallel Cut-Cell Cartesian CFD Code for Rapid Grid Generation Applied to In-Cylinder Diesel Engine Simulations," SAE Technical Paper 2007-01-0159 (2007). https://doi.org/10.4271/2007-01-015.
49. Quan, S. et al., *A One-Way Coupled Volume of Fluid and Eulerian-Lagrangian Method for Simulating Sprays* (Dec. 2016), doi:10.1115/ICEF2016-9390

Contact Information

Dr. Bret Windom
Bret.Windom@colostate.edu
P: (970) 491-7794
Department of Mechanical Engineering
Colorado State University
1374 Campus Delivery
Fort Collins, CO 80521, US

Acknowledgments

This research is funded by the U.S. Department of Energy under grant number DE-EE0009198.

Definitions/Abbreviations

AMR - Adaptive mesh refinement
ASI - After start of injection
C:H - Carbon to hydrogen ratio
C_A - Cone angle
CFD - Computational fluid dynamics
CNG - Compressed natural gas
DI - Direct injection
DISI - Direct injected, spark ignited
DME - Dimethyl ether
ECN - Engine Combustion Network
GDI - Gasoline direct injection
GHG - Greenhouse gases
HPSC - High-pressure spray chamber
HRM - Homogenous relaxation model
I_A - Inclusion angle
ICE - Internal combustion engine
$I_{Sch,norm}$ - Normalized Schlieren intensity
KH-RT - Kelvin Helmotz Rayleigh Taylor model
LECM - Large engine control module
LES - Large eddy simulation
LPG - Liquified petroleum gas
Nd: YAG - Neodymium-doped yttrium aluminum garnet laser
P_{amb} - Ambient pressure
P_{inj} - Injection pressure
PISO - Pressure implicit with splitting of operators method
P_{sat} - Saturation pressure
RT - Rayleigh Taylor model
T_{amb} - Ambient temperature
T_{fuel} - Fuel temperature
URANS - Unsteady Reynolds-average

ISSN 0148-7191